Aalborg Universitet

AALBORG UNIVERSITY

DENMARK

Modeling and Analysis of Harmonic Stability in an AC Power-Electronics-Based Power System

Wang, Xiongfei; Blaabjerg, Frede; Wu, Weimin

Publication date:
2014

Document Version
Early version, also known as pre-print

Link to publication from Aalborg University

Modeling and Analysis of Harmonic Stability in an AC Power-Electronics-Based Power System

Xiongfei Wang, *Member, IEEE*, Frede Blaabjerg, *Fellow, IEEE*, and Weimin Wu

Abstract—**This paper addresses the harmonic stability caused by the interactions among the wideband control of power converters and passive components in an AC power-electronics-based power system. The impedance-based analytical approach is employed and expanded to a meshed and balanced three-phase network which is dominated by multiple current- and voltage- controlled inverters with *LCL*- and *LC*-filters. A method of deriving the impedance ratios for different inverters is proposed by means of the nodal admittance matrix, and thus the contribution of each inverter to the harmonic stability of the overall power system can be easily predicted through Nyquist diagrams. Time-domain simulations and experimental tests on a three-inverter-based power system are presented. The results validate the effectiveness of the theoretical approach.**

Index Terms—**Current-controlled inverter, voltage-controlled inverter, impedance-based analysis, harmonic stability, power-electronics-based power system**

I. INTRODUCTION

The proportion of power electronics apparatus in electric power systems keeps growing in recent years, driven by the rapid development of renewable power sources and variable-speed drives [1]. As a consequence, power-electronics-based power systems are becoming important components of electrical grids, such as renewable power plants [2], [3], microgrids [4], and electric railway systems [5]. These systems possess superior features to build the modern power grids, including the full controllability, the sustainability, and the improved efficiency, but bring also new challenges. High-order harmonics tend to be aggravated by the high-frequency switching operation of power converters, which may trigger the parallel and series resonance in the power system [6]. The interactions of the wideband control systems for power converters with each other and with passive components may manifest instability phenomena of a power-electronics-based power system in the different frequency ranges [2]-[5].

Continuous research efforts have been made to investigate the instability in AC power-electronics-based power systems.

However, many of the studies focus on the low-frequency oscillations caused by the constant power control for converters as constant power loads [7]-[9] or constant power generators [10], [11], the Phase-Locked Loop (PLL) for grid-connected converters [12]-[14], and the droop-based power control for converters in islanded microgrids [15]-[17]. Apart from such oscillations associated with the outer power control and grid synchronization loops, the interactions of the fast inner current or voltage control loops may also result in harmonic instability phenomena, namely harmonic-frequency oscillations (typically from hundreds of Hz to several kHz), due to the inductive or capacitive behavior of converters in this frequency range [18]-[22]. Further, this harmonic instability may also be generated or magnified by the control of converters in interaction with harmonic resonance conditions introduced by the high-order power filters for converters and parasitic capacitors of power cables [23]-[26]. Such phenomena have been frequently reported in renewable energy systems and high-speed railway [2], [3], [5], [26]-[30], and are challenging the system stability and power quality. It is therefore important to develop the effective modeling and analysis approach for the harmonic stability problem in AC power-electronics-based power systems.

A general analytical approach for the harmonic stability problem is to build the state-space model of the power system, and identify the oscillatory modes based on the eigenvalues and eigenvectors of the state matrix [31]. However, unlike conventional power systems where the dynamics are mainly determined by the rotating machines, the small time constants of power converters require the detailed models of loads and network dynamics in power-electronics-based power systems [7]. Thus, the formulation of the system matrices may become complicated, and the virtual resistors are usually needed to avoid the ill-conditioned problems [32]. To overcome these limits, the Component Connection Method (CCM) is introduced for the stability analysis of AC power systems including the High-Voltage Direct Current (HVDC) transmission lines [33]. The CCM is basically a particular form of state-space models, where the power system components and network dynamics are separately modeled by a set of two vector-matrix equations. This results in the sparsity of the state equations and reduces the computation burden of formulating the system transfer matrices. Further, the component interactions and the critical system parameters for the different oscillatory modes can be more easily determined [34], [35].

Apart from the state-space analysis, the impedance-based approach, which is originally introduced for the design of input filters in DC-DC converters [36], provides another attractive way to analyze the harmonic stability problem. Similarly to the CCM, the impedance-based analysis is also built upon the models of components or subsystems. However, instead of systematically analyzing the eigenproperties of the state matrix as in the CCM and other state-space models, the impedance-based approach locally predicts the system stability at each Point of Connection (PoC) of component, based on the ratio of the output impedance of component and the equivalent system impedance [37]. Thus, the formulation of the system matrices can be avoided, and the contribution of each component to the system stability can be readily assessed in the frequency-domain. Also, the output impedance of component or subsystem can be accordingly reshaped to stabilize the overall power system [38]. Therefore, the impedance-based method provides a more straightforward and design-oriented stability analysis compared to the CCM and other state-space models. Several applications of the impedance-based approach for the harmonic stability analysis can be found in AC power-electronics-based power systems, e.g. the cascaded sour-load inverter system [39], the parallel grid-connected converters with *LCL*-filters [22], and the parallel uninterruptible power supply inverters with *LC*-filters [25]. However, in all these cases, the network dynamics are often overlooked which affect the derivation of the equivalent system impedance, and few of them have considered the systems with multiple voltage- and current-controlled converters.

This paper attempts to fill in this gap by expanding the impedance-based analysis to a three-phase meshed and balanced power system, where a voltage-controlled and two current-controlled inverters with *LC*- and *LCL*-filters are interconnected. The harmonic instability that results from the interactions among the inner voltage and current control loops of these inverters and passive components is studied, while the dynamic impacts of the outer power control and grid synchronization loops are neglected by designing the control bandwidth lower than the system fundamental frequency. By the help of the nodal admittance matrix, a simple method of deriving the impedance ratio at the PoC of inverters is proposed to assess how each inverter contributes to the harmonic instability of the power system. The theoretical analysis in the frequency-domain is performed based on the linearized models of inverters with inner control loops. The results are further validated by the nonlinear time-domain simulations and experimental tests on a three-inverter-based power system.

II. SYSTEM MODELING AND ANALYSIS TECHNIQUES

This section first describes the structure of the built power-electronics-based power system in this work, and then reviews the CCM and the impedance-based approach for modeling and
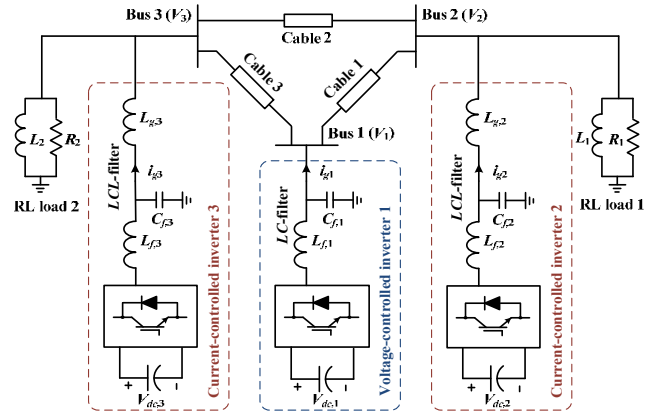

Fig. 1. Simplified one-line diagram of a three-phase power-electronics-based AC power system.

analysis of harmonic stability in the power system.

A. System Description

Fig. 1 shows a simplified one-line diagram for the balanced three-phase power-electronics-based power system which is considered in this work, where a voltage-controlled and two current-controlled inverters are interconnected as a meshed power network through power cables. The voltage-controlled inverter regulates the system frequency and voltage amplitude. The current-controlled inverters operate with unity power factor. In such a system, the presence of shunt capacitors in the *LC*- and *LCL*-filters of inverters and power cables brings in resonant frequencies, which may interact with the inner voltage and current control loops of voltage- and current-controlled inverters resulting in the harmonic-frequency oscillations and unexpected harmonic distortion. On the other hand, the dynamic interactions between the inner control loops of inverters may also trigger the existing resonant frequencies in the power system. This consequently necessitates the use of CCM or impedance-based analysis to reveal how inverters interact with each other and with the harmonic resonance conditions in the system.

Since this work is concerned with the harmonic instability owing to the dynamics of inner control loops, the DC-link voltages of inverters are assumed to be constant. Also, the grid synchronization loop for the current-controlled inverters is designed with the bandwidth lower than system fundamental frequency, thus only the subsynchronous oscillation may be induced by grid synchronization [12]-[14]. Under these assumptions, only the inner voltage and current control loops are modeled in this work. The previous studies have shown that the inner control loops themselves can be simply modeled by the single-input and single-output transfer functions in the stationary $\alpha\beta$-frame [20], [25]-[27], [39]-[43].

B. CCM

Fig. 2 shows the block diagram of the CCM applied for the built power system, where the CCM decomposes the overall system into three subsystems by inverters and the connection
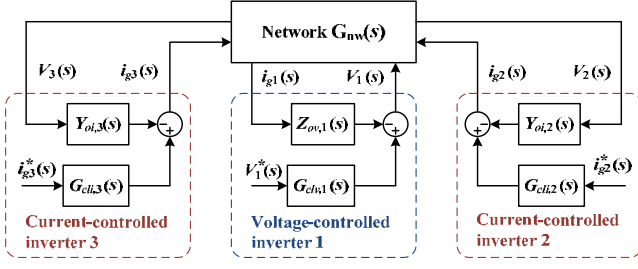
Fig. 2. Block diagram of the CCM applied for the built power system.

network. Two current-controlled inverters are modeled by the Norton equivalent circuits [22], while the voltage-controlled inverter is represented by the Thevenin equivalent circuit [23]. Consequently, the composite inverter model can be derived in the following

$$y(s) = \mathbf{G_{cl}}(s)u(s) - \mathbf{G_{cd}}(s)d(s) \tag{1}$$

where $y(s)$ and $d(s)$ are the output vector and disturbance vector of inverters, respectively.

$$y(s) = [V_1(s), i_{g2}(s), i_{g3}(s)]^{\mathrm{T}} \tag{2}$$

$$u(s) = [V_1^*(s), i_{g2}^*(s), i_{g3}^*(s)]^{\mathrm{T}} \tag{3}$$

$\mathbf{G_{cl}}$ **(s)** and $\mathbf{G_{cd}}$ **(s)** denote the closed-loop reference-to-output and the closed-loop disturbance-to-output transfer matrices, respectively, which depict the unterminated dynamic behavior of inverters seen from the PoC and can be given by

$$\mathbf{G_{cl}}(s) = \mathrm{diag}[G_{clv,1}(s), G_{cli,2}(s), G_{cli,3}(s)] \tag{4}$$

$$\mathbf{G_{cd}}(s) = \mathrm{diag}[Z_{ov,1}(s), Y_{oi,2}(s), Y_{oi,3}(s)] \tag{5}$$

where $G_{clv,1}(s)$, $G_{cli,2}(s)$, and $G_{cli,3}(s)$ are the voltage and current reference-to-output transfer functions of voltage- and current-controlled inverters, respectively. $Z_{ov,1}(s)$, $Y_{oi,2}(s)$, and $Y_{oi,3}(s)$ are the closed-loop output impedance and admittances of the voltage- and current-controlled inverters, respectively.

The dynamic of the connection work can be represented by the transfer matrix $\mathbf{G_{nw}}$ **(s)** as

$$d(s) = \mathbf{G_{nw}}(s)y(s) \tag{6}$$

Thus, the closed-loop response of the overall power system can be derived as

$$y(s) = [\mathbf{I} + \mathbf{G_{nw}}(s)\mathbf{G_{cd}}(s)]^{-1}\mathbf{G_{cl}}(s)u(s) \tag{7}$$

where the transfer matrix $[\mathbf{I} + \mathbf{G_{nw}(s)G_{cd}(s)}]^{-1}$ predicts the harmonic instability of the power system, provided that the unterminated behavior of inverters $\mathbf{G_{cl}}$ **(s)** are stable. In

addition to the eigenvalues technique, the transfer matrix can also be evaluated in the multivariable frequency-domain by means of the generalized Nyquist stability criterion [44], [45].

It is obvious that the main superior feature of the CCM compared to the other state-space models is to decompose the power system into multiple decentralized feedback loops by inverters, and thus the effect of inverters controllers and the associated physical components on the system oscillatory modes is more intuitively revealed. Further, the decentralized stabilizing control loops may be developed by means of the CCM [46].

C. *Impedance-Based Approach*

Fig. 3 depicts the equivalent circuits of the voltage- and current-controlled inverters applied for the impedance-based analysis. It is interesting to note that this approach also separately models the internal dynamics of inverters by means of the output impedance and admittance. However, differently from the CCM, there is no need of stacking the reference-to-output and disturbance-to-output transfer functions of inverters as transfer matrices in the impedance-based approach [38]. Instead, the impact of a given inverter on the overall system stability is determined by a minor feedback loop composed by the ratio of the inverter output impedance or admittance, $Z_{ov,1}$ or $Y_{oi,m}$ and the equivalent impedance or admittance for the rest of the system, $Z_{lv,1}$ or $Y_{li,m}$ [40]. Further, due to the scalar type models for inner control loops of inverters, the impedance ratios can also be depicted by single-input and single-output transfer functions [39], which significantly simplify the harmonic stability analysis compared to the CCM and other state-space models. Hence, the impedance-based approach is preferred in this work.

From Fig. 3, the closed-loop transfer functions of inverters can be derived as follows

$$\frac{V_1(s)}{V_1^*(s)} = G_{clv,1}(s)\frac{1}{1+\dfrac{Z_{ov,1}(s)}{Z_{lv,1}(s)}} \tag{8}$$

$$\frac{i_{gm}(s)}{i_{gm}^*(s)} = G_{cli,m}(s)\frac{1}{1+\dfrac{Y_{oi,m}(s)}{Y_{li,m}(s)}} \tag{9}$$

It is clear that if the unterminated dynamic behavior of inverters, $G_{clv,1}$ and $G_{cli,m}$ are stable, the stability of voltage and current at the PoC of inverters will be dependent on the minor feedback loops composed by the following impedance ratios

$$T_{mv}(s) = \frac{Z_{ov,1}(s)}{Z_{lv,1}(s)}, \quad T_{mc}(s) = \frac{Y_{oi,m}(s)}{Y_{li,m}(s)} \tag{10}$$

which are also termed as the minor feedback loop gains [40]. Based on these minor feedback loop gains, the specifications
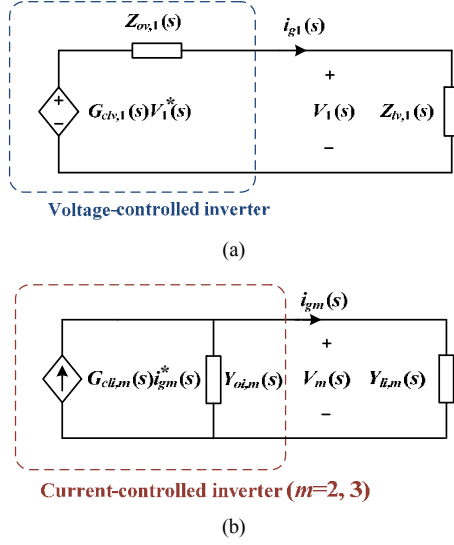
Fig. 3. Impedance-based equivalent models for (a) the voltage- and (b) current-controlled inverters.

of inverters output impedances to preserve the system stability can be derived.

III. MODELING OF INVERTERS

A. Voltage-Controlled Inverters

Fig. 4 depicts the simplified one-line diagram of voltage-controlled inverter and the multiloop voltage control scheme. The control system is implemented in the stationary frame, including the inner Proportional (P) current controller and outer Proportional Resonant (PR) voltage controller. It is worth mentioning that the three-phase inverters without neutral wire can be transformed into two independent single-phase systems in the stationary $\alpha\beta$-frame [42]. Further, due to the assumptions of the constant DC-link voltage and balanced three-phase operation, the voltage-controlled inverter can be linearized based on the LC-filter and modeled as a real scalar system by single-input and single-output transfer functions [23]-[25], [42], [43].

Fig. 5 shows the block diagram of the multiloop voltage control system, where the following two transfer functions are used to describe the effect of the inverter output voltage $V_{PWM,1}$ and grid current i_{g1} on the filter inductor current i_{L1}, respectively.

$$Y_{Li}(s) = \frac{1}{Z_{Lf,1}(s) + Z_{Cf,1}(s)}, \quad G_{ii}(s) = \frac{Z_{Cf,1}(s)}{Z_{Lf,1}(s) + Z_{Cf,1}(s)} \quad (11)$$

where $Z_{Lf,1}(s)$ and $Z_{Cf,1}(s)$ are the impedances of the filter inductor and capacitor, respectively. Thus, the dynamic behavior of the inner current control loop can be given by

$$i_{L1}(s) = \frac{T_{c,1}(s)}{1 + T_{c,1}(s)} i_{L1}^*(s) + \frac{G_{ii}(s)}{1 + T_{c,1}(s)} i_{g1}(s) \quad (12)$$
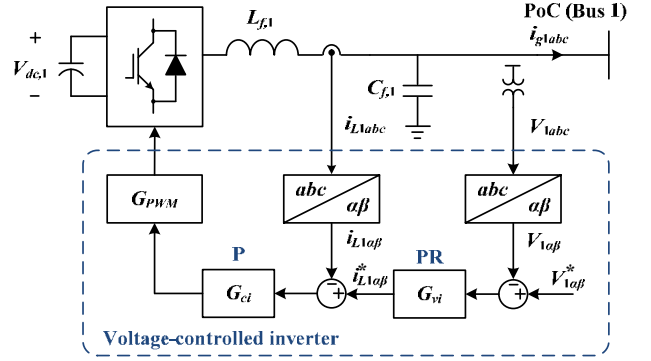

Fig. 4. Voltage-controlled inverter with the multiloop control scheme.
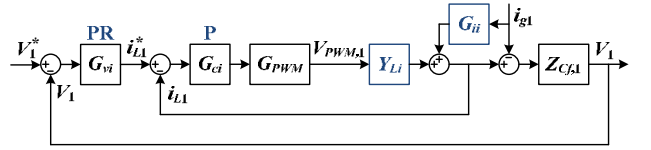

Fig. 5. Block diagram of the multiloop voltage control system.

where $T_{c,1}(s)$ is the open-loop gain of the inner current control loop, which is expressed as

$$T_{c,1}(s) = G_{ci}(s)G_{PWM}(s)Y_{Li}(s) \quad (13)$$

$$G_{ci}(s) = K_{pi}, \quad G_{PWM}(s) = e^{-j1.5T_s s} \quad (14)$$

where $G_{ci}(s)$ is the P current controller and $G_{PWM}(s)$ depicts the effect of the digital computation delay (T_s) and the Pulse Width Modulation (PWM) delay ($0.5T_s$) [42]. Then, by including the outer voltage control loop, the voltage reference-to-output transfer function and closed-loop output impedance are derived in the following

$$V_1(s) = G_{clv,1}(s)V_1^*(s) - Z_{ov,1}(s)i_{g1}(s) \quad (15)$$

$$G_{clv,1}(s) = \frac{T_v(s)}{1 + T_v(s)}, \quad Z_{ov,1}(s) = \frac{Z_{oi}(s)}{1 + T_v(s)} \quad (16)$$

$$T_v(s) = \frac{G_{vi}(s)G_{ci}(s)G_{PWM}(s)Z_{Cf,1}(s)}{Z_{Lf,1}(s) + Z_{Cf,1}(s) + G_{ci}(s)G_{PWM}(s)} \quad (17)$$

$$Z_{oi}(s) = \frac{Z_{Cf,1}(s)\left[Z_{Lf,1}(s) + G_{ci}(s)G_{PWM}(s)\right]}{Z_{Lf,1}(s) + Z_{Cf,1}(s) + G_{ci}(s)G_{PWM}(s)} \quad (18)$$

$$G_{vi}(s) = K_{pv} + \frac{K_{rv}s}{s^2 + \omega_1^2} \quad (19)$$

where $G_{vi}(s)$ is the PR voltage controller and ω_1 denotes the system fundamental frequency. $T_v(s)$ is the open-loop gain of

the control system. $Z_{oi}(s)$ is the open-loop output impedance obtained with the outer voltage control loop open and the inner current loop closed.

B. Current-Controlled Inverters

Fig. 6 shows the simplified one-line diagram of the current-controlled inverters and the associated control system. The grid-side inductor current of the *LCL*-filter is controlled for the inherent resonance damping effect of the computation and modulation delays [47]. The PR controller in the stationary *αβ*-frame is adopted for grid current control. The synchronous reference frame PLL is used for grid synchronization [48].

It is important to mention that the PLL has an important effect on the output admittance of inverter in addition to the current control loop. The inclusion of PLL effect will introduce an unbalanced three-phase inverter model which needs to be described by transfer matrices [12]. However, it has been found in recent studies that the PLL only affects the output admittance within its control bandwidth where the negative resistance behavior may be introduced [14], and this problem can be avoided by reducing the bandwidth of PLL [13]. Hence, in this work, the bandwidth of the PLL is designed to be lower than the system fundamental frequency in order not to bring in any harmonic-frequency oscillations. Thus, the current control loop itself is linearized based on the *LCL*-filter and is modeled as a real scalar system.

Fig. 7 depicts the block diagram of the grid current control loop. The *LCL*-filter in itself is a two-input and single-output system, where the PoC voltage V_m and inverter output voltage $V_{PWM,m}$ are the two inputs and grid current i_{gm} is the output. Thus, the following two transfer functions are used to model the *LCL*-filter plant.

$$Y_{gi,m}(s) = \frac{i_{gm}(s)}{V_{PWM,m}(s)}\bigg|_{V_m(s)=0} = \frac{Z_{Cf,m}(s)}{Z_{Cf,m}(s)Z_{Lf,m}(s) + Z_{Lg,m}(s)Z_{Lf,m}(s) + Z_{Cf,m}(s)Z_{Lg,m}(s)} \tag{20}$$

$$Y_{o,m}(s) = \frac{i_{gm}(s)}{V_m(s)}\bigg|_{V_{PWM,m}(s)=0} = \frac{Z_{Lf,m}(s) + Z_{Cf,m}(s)}{Z_{Cf,m}(s)Z_{Lf,m}(s) + Z_{Lg,m}(s)Z_{Lf,m}(s) + Z_{Cf,m}(s)Z_{Lg,m}(s)} \tag{21}$$

where $Z_{Lf,m}(s)$, $Z_{Lg,m}(s)$ and $Z_{Cf,m}(s)$ denote the impedances of the *LCL*-filter inductors and capacitor, respectively. $Y_{o,m}(s)$ is the open-loop output admittance. From Fig. 7, the closed-loop response of the current control loop can be derived as follows

$$i_{gm}(s) = G_{cli,m}(s)i_{gm}^*(s) - Y_{oi,m}(s)V_m(s) \tag{22}$$

$$G_{cli,m}(s) = \frac{T_{c,m}(s)}{1 + T_{c,m}(s)}, \quad Y_{oi,m}(s) = \frac{Y_{o,m}(s)}{1 + T_{c,m}(s)} \tag{23}$$
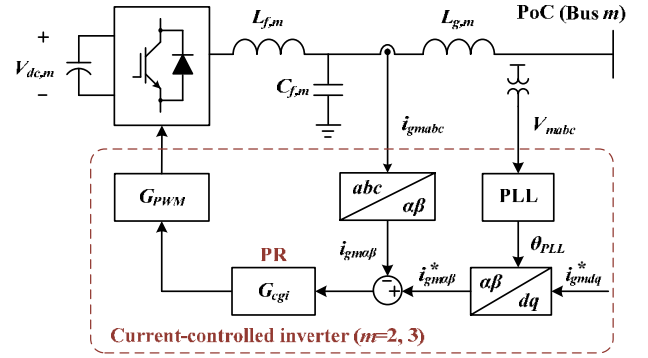

Fig. 6. Current-controlled inverter (*m*=2, 3) with grid current control scheme.
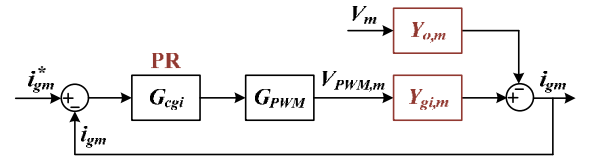

Fig. 7. Block diagram of the grid current control loop.

where $G_{cli,m}(s)$ and $Y_{oi,m}(s)$ are the current reference-to-output transfer function and closed-loop output admittance, respectively. $T_{c,m}(s)$ is the open-loop gain of current control loop, which is given by

$$T_{c,m}(s) = G_{cgi}(s)G_{PWM}(s)Y_{gi,m}(s) \tag{24}$$

$$G_{cgi}(s) = K_{pgi} + \frac{K_{rgi}s}{s^2 + \omega_1^2} \tag{25}$$

where $G_{cgi}(s)$ is the PR current controller.

IV. ANALYSIS OF HARMONIC STABILITY

To perform the impedance-based analysis of harmonic stability in the built power system, a method of deriving the impedance ratio at each PoC of inverter is proposed in this section. It is noted from Fig. 3 that the equivalent system impedance seem from the PoC of inverter is indispensable in the impedance ratio. Hence, an equivalent system impedance derivation procedure is developed by the help of the nodal admittance matrix and used in the following analysis.

A. System Equivalent Circuit

Fig. 8 depicts the impedance-based equivalent circuit for the power system shown in Fig. 1. The power cables are represented as the Π-section models to include the effect of parasitic capacitors. Also, to facilitate the formulation of nodal admittance matrix, the Thevenin model of voltage-controlled inverter is converted to the Norton circuit where $Y_{ov,1}=1/Z_{ov,1}$.

To obtain the equivalent system impedance at each PoC of inverter, the system nodal admittance matrix ($\mathbf{Y_{nc}}$) including the closed-loop output admittances of inverters, as highlighted
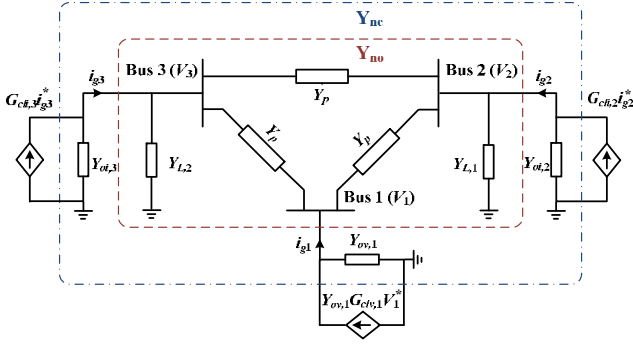
Fig. 8. Impedance-based equivalent circuit for the built power system.

by the dot-dashed line in Fig. 8, is derived as

$$\begin{bmatrix} Y_{ov,1}G_{clv,1}V_1^* \\ G_{cli,2}i_{g2}^* \\ G_{cli,3}i_{g3}^* \end{bmatrix} = \mathbf{Y_{nc}} \begin{bmatrix} V_1 \\ V_2 \\ V_3 \end{bmatrix} \tag{26}$$

$$\mathbf{Y_{nc}} = \begin{bmatrix} Y_{ov,1} + 2Y_p & -Y_p & -Y_p \\ -Y_p & Y_{oi,2} + 2Y_p + Y_{L,1} & -Y_p \\ -Y_p & -Y_p & Y_{oi,3} + 2Y_p + Y_{L,2} \end{bmatrix} \tag{27}$$

where Y_p is the cable admittance, $Y_{L,1}$ and $Y_{L,2}$ are the admittances for loads 1 and 2 connected to Buses 2 and 3, respectively. Then, by inverting $\mathbf{Y_{nc}}$, the nodal impedance matrix ($\mathbf{Z_{nc}}$) is given by

$$\mathbf{Z_{nc}} = \mathbf{Y_{nc}^{-1}} = \begin{bmatrix} Z_{11} & Z_{12} & Z_{13} \\ Z_{21} & Z_{22} & Z_{23} \\ Z_{31} & Z_{32} & Z_{33} \end{bmatrix} \tag{28}$$

where the elements are expanded in (29).

It is worth noting that the diagonal elements of the nodal

impedance matrix are the equivalent system impedances seen from the equivalent current sources of inverters, which include the closed-loop output impedances of inverters and the equivalent system impedances at the PoC of inverters. Consequently, the equivalent system impedances at the PoC of inverters can be derived by the following relationship

$$Z_{11} = \frac{Z_{ov,1}Z_{lv,1}}{Z_{ov,1} + Z_{lv,1}}, \quad Z_{22} = \frac{1}{Y_{oi,2} + Y_{li,2}}, \quad Z_{33} = \frac{1}{Y_{oi,3} + Y_{li,3}} \tag{30}$$

Further, comparing the term Z_{11} in (30) with (8), it is seen that the closed-loop response of the voltage-controlled inverter can also be expressed by

$$\frac{V_1(s)}{V_1^*(s)} = G_{clv,1}(s)Z_{11}(s)Y_{ov,1}(s) \tag{31}$$

where $Z_{11}Y_{ov,1}$ is the closed-loop gain of the minor feedback loop. Similarly, the closed-loop responses of the current-controlled inverters can also be found by means of the nodal admittance matrix ($\mathbf{Y_{no}}$) derived at the PoC of inverters, which is highlighted by the dashed line in Fig. 8.

$$\begin{bmatrix} i_{g1} \\ i_{g2} \\ i_{g3} \end{bmatrix} = \underbrace{\begin{bmatrix} 2Y_p & -Y_p & -Y_p \\ -Y_p & 2Y_p + Y_{L,1} & -Y_p \\ -Y_p & -Y_p & 2Y_p + Y_{L,2} \end{bmatrix}}_{\mathbf{Y_{no}}} \begin{bmatrix} V_1 \\ V_2 \\ V_3 \end{bmatrix} \tag{32}$$

Together with (26), (28) and (29), the closed-loop response of the equivalent current sources can be derived as

$$\begin{bmatrix} i_{g,1} \\ i_{g2} \\ i_{g3} \end{bmatrix} = \mathbf{Y_{no}Z_{nc}} \begin{bmatrix} Y_{ov,1}G_{clv,1}V_1^* \\ G_{cli,2}i_{g2}^* \\ G_{cli,3}i_{g3}^* \end{bmatrix} \tag{33}$$

$$Z_{11} = \frac{Y_{oi,2}Y_{oi,3} + Y_{oi,2}Y_{L,2} + Y_{oi,3}Y_{L,1} + 2Y_{oi,2}Y_p + 2Y_{oi,3}Y_p + Y_{L,1}Y_{L,2} + 2Y_{L,1}Y_p + 2Y_{L,2}Y_p + 3Y_p^2}{Y_{nom}}$$

$$Z_{22} = \frac{Y_{ov,1}Y_{oi,3} + Y_{ov,1}Y_{L,2} + 2Y_{ov,1}Y_p + 2Y_{oi,3}Y_p + 2Y_{L,2}Y_p + 3Y_p^2}{Y_{nom}}$$

$$Z_{33} = \frac{Y_{ov,1}Y_{oi,2} + Y_{ov,1}Y_{L,1} + 2Y_{ov,1}Y_p + 2Y_{oi,2}Y_p + 2Y_{L,1}Y_p + 3Y_p^2}{Y_{nom}} \tag{29}$$

$$Z_{12} = Z_{21} = \frac{Y_{oi,3}Y_p + Y_{L,2}Y_p + 3Y_p^2}{Y_{nom}}, \quad Z_{13} = Z_{31} = \frac{Y_{oi,2}Y_p + Y_{L,1}Y_p + 3Y_p^2}{Y_{nom}}, \quad Z_{23} = Z_{32} = \frac{Y_{ov,1}Y_p + 3Y_p^2}{Y_{nom}}$$

$$Y_{nom} = 3Y_p^2(Y_{ov,1} + Y_{oi,2} + Y_{oi,3} + Y_{L,1} + Y_{L,2}) + 2Y_p(Y_{ov,1}Y_{oi,2} + Y_{ov,1}Y_{oi,3} + Y_{ov,1}Y_{L,1} + Y_{ov,1}Y_{L,2})$$

$$+ (2Y_p + Y_{ov,1})(Y_{oi,2}Y_{oi,3} + Y_{oi,2}Y_{L,2} + Y_{oi,3}Y_{L,1} + Y_{L,1}Y_{L,2})$$

Comparing (33) with (9), it can be found that the second and third diagonal elements of the closed-loop transfer matrix $\mathbf{Y_{no}Z_{nc}}$ represent the closed-loop gains of the minor feedback loops for the current-controlled inverters.

B. Impedance-Based Analysis

Table I lists the main electrical parameters of the studied power system. Table II gives the parameters of the voltage and current controllers for inverters. The cables use the same Π-section models, and two current-controlled inverters are also designed with the same parameters for the sake of simplicity.

Fig. 9 shows the frequency responses of inner control loop gains, $T_v(s)$ and $T_{c,m}(s)$, for the voltage- and current-controlled inverters, respectively. The stable unterminated dynamic behaviors of inverters at the PoC are observed with the controllers parameters listed in Table II. This provides a theoretical basis for using the minor feedback loops to assess the harmonic stability of the power system.

TABLE I
MAIN ELECTRICAL PARAMETERS OF POWER SYSTEM

Electrical Constants		Values (p.u.[a])
Power cables (Π-section)	Series inductance (L_p)	0.005
	Seres resistance (R_p)	0.013
	Shunt capacitance (C_p)	0.01
RL load 1, 2	Resistance ($R_1=R_2$)	0.12
	Inductance ($L_1 =L_2$)	5.06
Voltage-controlled inverter 1	Filter inductor ($L_{f,1}$)	0.03
	Filter capacitor ($C_{f,1}$)	0.13
	DC-link voltage ($V_{dc,1}$)	1.88
Current-controlled inverter 2, 3	Filter inductor ($L_{f,2}= L_{f,3}$)	0.3
	Filter capacitor ($C_{f,2}= C_{f,3}$)	0.024
	Filter inductor ($L_{g,2}= L_{g,3}$)	0.035
	DC-link voltage ($V_{dc,2} =V_{dc,3}$)	1.88
	Active power ($P_2 = P_3$)	0.1
	Reactive power ($Q_2 = Q_3$)	0

a. System PU base voltage: 400 V, base frequency: 50 Hz, and base power: 10 kVA.

TABLE II
CONTROLLER PARAMETERS OF INVERTERS

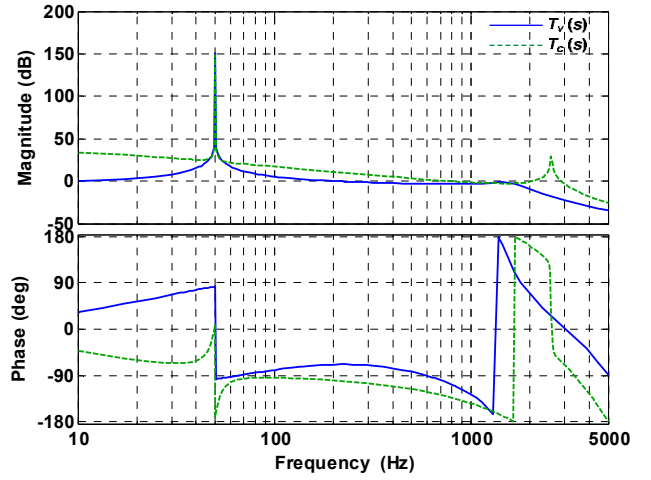| Controllers parameters			Values
Voltage-controlled inverter 1	Current controller	K_{pi}	8
	Voltage controller	K_{pv}	0.1
		K_{rv}	100
	Sampling period	$T_{d,1}$	100 µs
Current-controlled inverter 2, 3	Current controller	$K_{pgi,2}= K_{pgi,3}$	15
		$K_{rgi,2}= K_{rgi,3}$	600
	Sampling period	$T_{d,2}= T_{d,3}$	100 µs

Fig. 9. Frequency responses for the open-loop gains of the voltage-controlled inverter, $T_v(s)$, and the current-controlled inverters, $T_c(s)$.

Fig. 10 depicts the Nyquist diagrams of the minor feedback loop gains of the voltage- and current-controlled inverters. Since the impedance ratios are described by single-input and single-output transfer functions, the Nyquist stability criterion can be directly used to evaluate the interactions among the inner control loops of inverters and the network dynamics. It is seen that the minor feedback loop for the voltage-controlled inverter is unstable whereas the minor feedback loops for the current-controlled inverters are stable. This implies that the impedance interaction at the PoC of the voltage-controlled inverter (Bus 1) causes the harmonic instability in the power system, and the admittance interactions at the PoC of current-controlled inverters have no contribution to the harmonic instability.

Fig. 11 shows the Nyquist diagrams of the minor feedback loop gains after adjusting the controller parameters for the voltage-controlled inverter. In this case, the proportional gains of the P current controller and the PR voltage controller are reduced (K_{pi} =5, K_{pv}=0.05). It is clear that all minor feedback loops become stable. This fact again indicates that the voltage-controlled inverter with the controller parameters given in Table II causes the harmonic instability in the power system even if it has a stable unterminated dynamic behavior.

V. SIMULATION AND EXPERIMENTAL RESULTS

To validate the impedance-based stability analysis in the frequency-domain, the power system in Fig. 1 is built in the nonlinear time-domain simulations by using MATLAB and PLECS Blockset, and the experimental tests.

A. Simulation Results

Fig. 12 shows the simulated grid currents of inverters with the electrical constants and controller parameters given in Tables I and II. The simulated bus voltages are shown in Fig. 13. It is seen that the harmonic-frequency oscillation occurs in the power system, which is confirms the frequency-domain
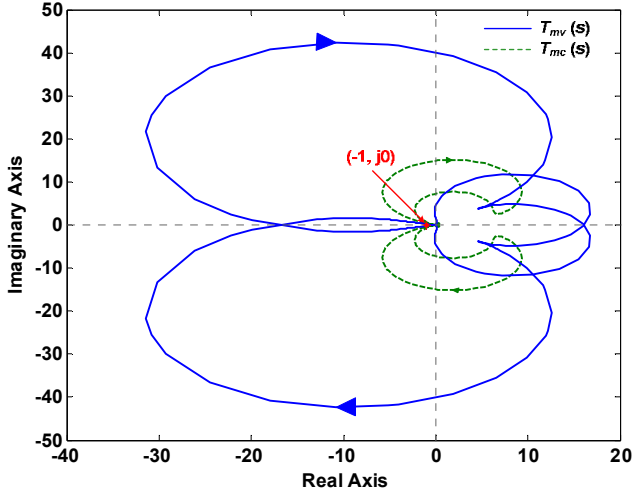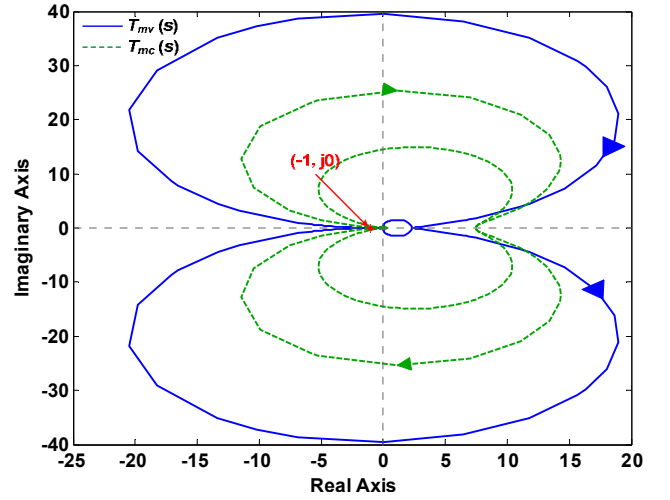
(a)
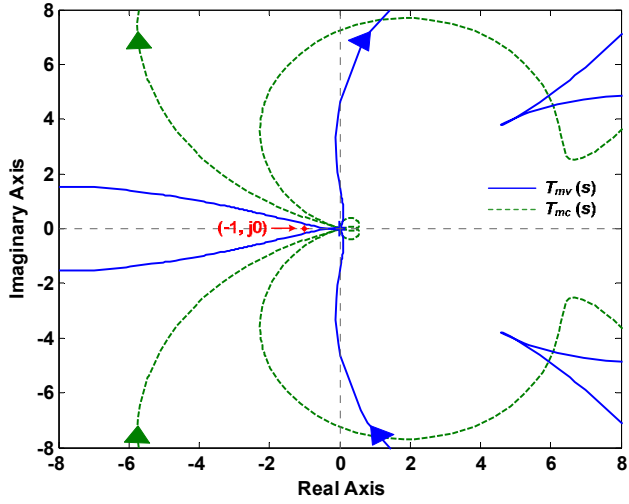
(b)

Fig. 10.   Nyquist plots of the minor feedback loop gains of inverters in the unstable case (a) Full view. (b) Zoom on (-1, j0).

(a)

(b)

Fig. 11.   Nyquist plots of the minor feedback loop gains of inverters in the stable case (a) Full view. (b) Zoom on (-1, j0).
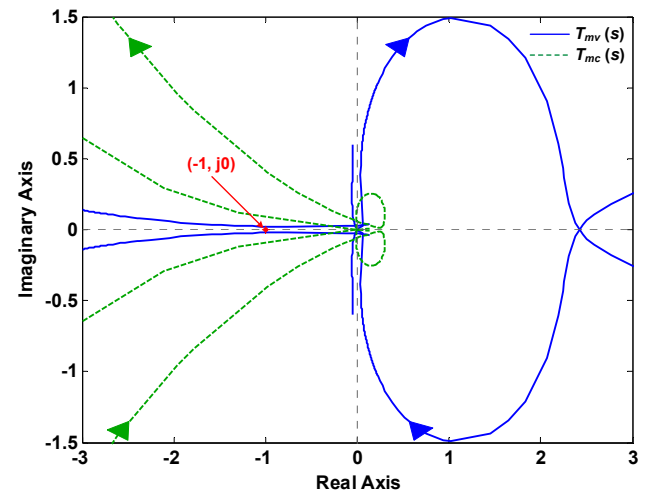
analysis in Fig. 10.

In contrast, Fig. 14 shows the simulated grid currents of inverters after reducing the proportional gains of controllers for the voltage-controlled inverter (K_{pi}=5, K_{pv}=0.05). The simulated voltage at each bus of the system is shown in Fig. 15. It is obvious that the harmonic instability phenomenon shown in Figs. 12 and 13 becomes stabilized in this case. This agrees well with the theoretical analysis in Fig. 11 and also verifies that the harmonic instability in the power system is caused by the voltage-controlled inverters rather than the current-controlled inverters.

B.   Experimental Results

Fig. 16 shows a hardware picture of the built power-electronics-based power system in laboratory. Three Danfoss frequency converters are employed to operate as a voltage-controlled inverter and two current-controlled inverters. The control algorithms of inverters are implemented in DS1006 dSPACE system, where the DS5101 digital waveform output board is adopted to generate switching pulses in synchronous with the sampling circuit [42]. The current transducer LA 55-P and voltage transducer LV 25-P are used to acquire current and voltage signals, respectively, for the digital control circuit.

In the experimental tests, the bus voltages of the power system and grid currents of inverters are recorded by using the digital oscilloscope with the 250-kS/s sampling rate and the 100-kHz effective bandwidth. The current probe with the 100-kHz bandwidth is adopted for the current measurement. The differential mode voltage probe with the 25-MHz bandwidth and maximum 1000-V Root Mean Square (RMS) is used for voltage measurement.

First, the unstable case that is based on the controller parameters given in Table II is tested. Figs. 17 and 18 depict
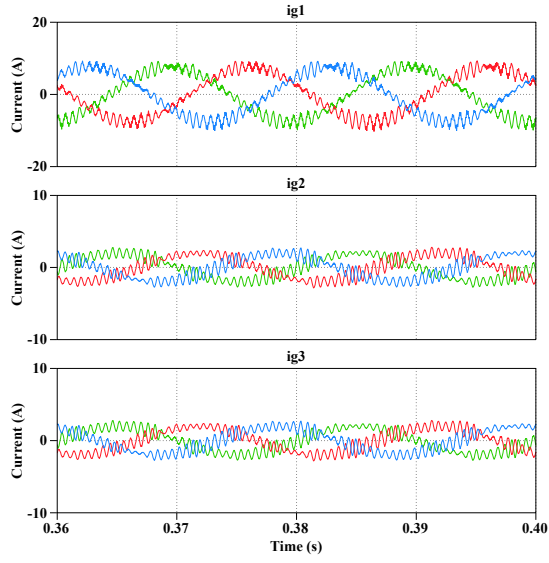
Fig. 12.   Simulated grid currents of inverters in the unstable case.
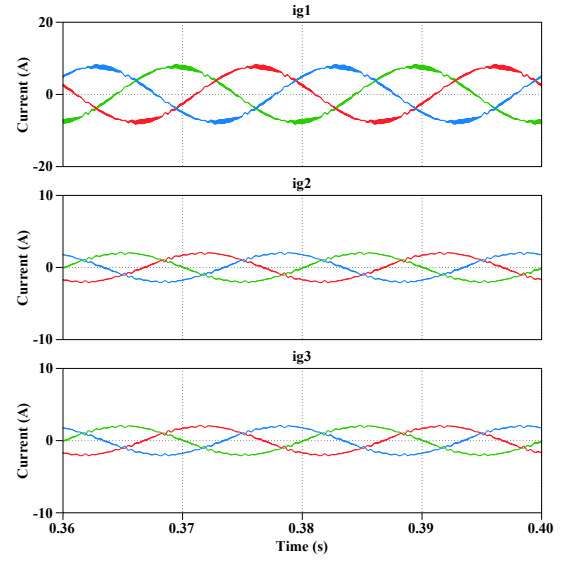

Fig. 14.   Simulated grid currents of inverters in the stable case.
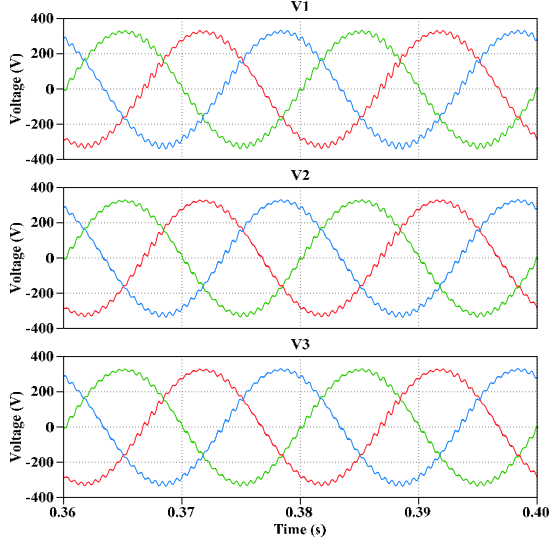

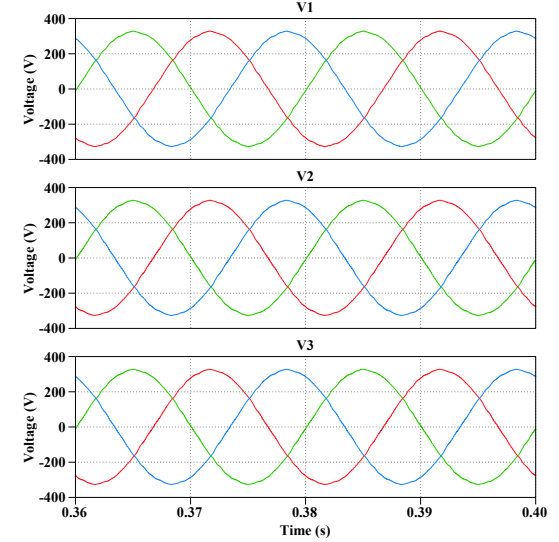Fig. 13.   Simulated bus voltages in the unstable case.

Fig. 15.   Simulated bus voltages in the stable case.

the measured grid currents of inverters and the measured bus voltages, respectively. It is observed that the same harmonic-frequency oscillation arises in the experimental test as in the simulation results shown in Figs. 12 and 13. Further, in both the simulation and experimental test, this harmonic-frequency oscillation propagates into the whole power system and leads to the unexpected harmonic disturbance to the current control loops of the current-controlled inverters. Consequently, even though no unstable condition is brought by the current-controlled inverters, as shown in Fig. 10, the harmonic-frequency oscillations are still present in the grid currents of current-controlled inverters. Hence, it is difficult to identify the source of harmonic instability in the power system by merely observing the simulations and experimental results. The impedance-based analysis in the frequency-domain thus
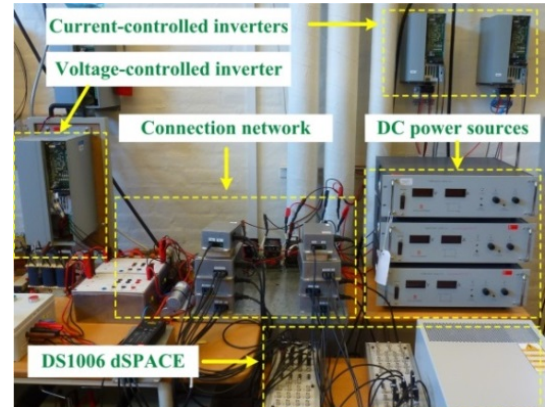

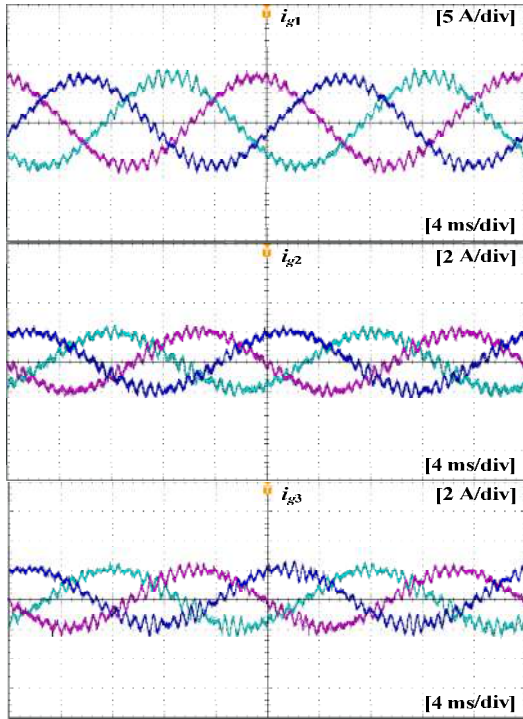Fig. 16.   Hardware picture of the built laboratory test setup.

Fig. 17. Measured grid currents of inverters in the unstable case.
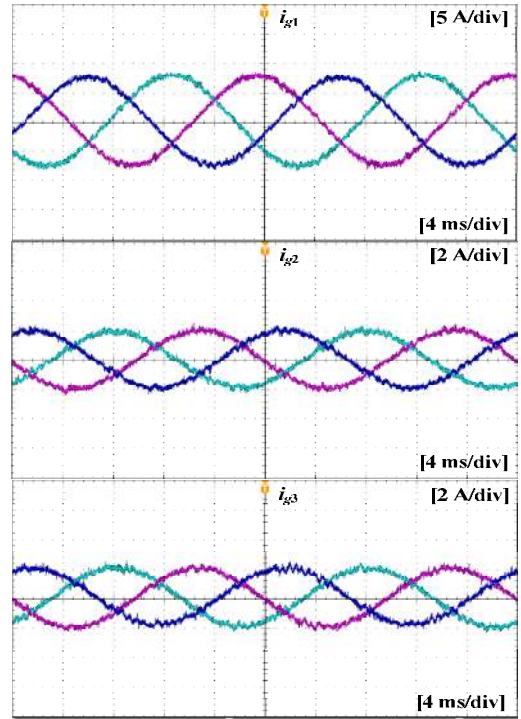
Fig. 19. Measured grid currents of inverters in the stable case.
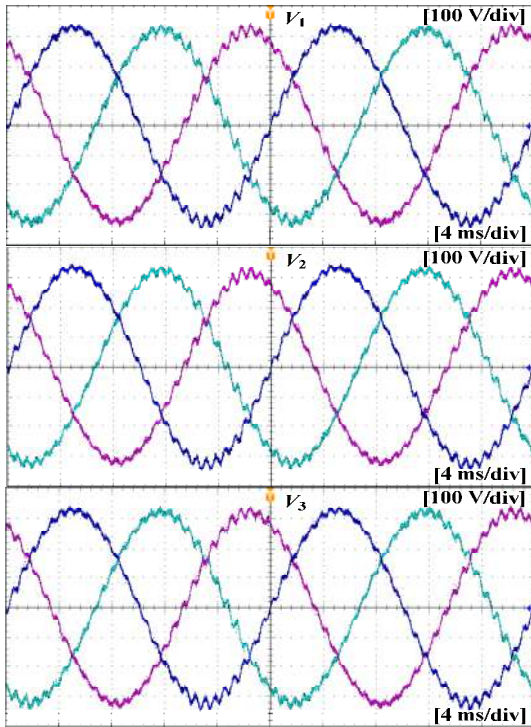
Fig. 18. Measured bus voltages in the unstable case.
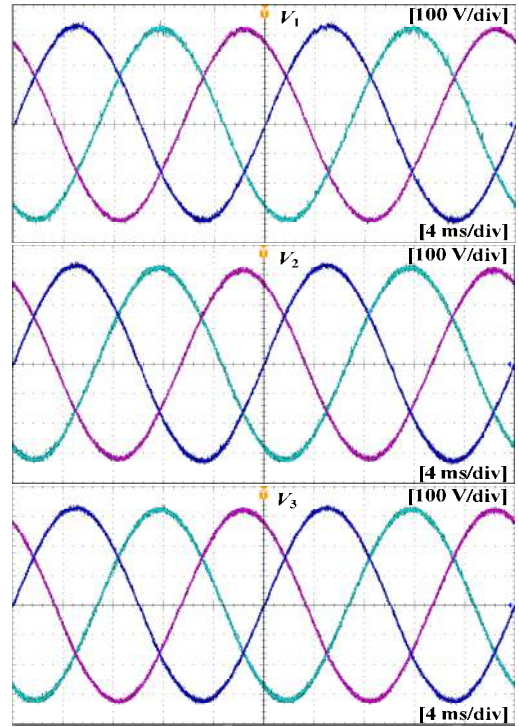
Fig. 20. Measured bus voltages in the stable case.

becomes important to reveal how each inverter contributes to the harmonic stability of the power system.

   Then, the stable case with the reduced proportional gains of the controllers for the voltage-controlled inverters (Kpi=5,

Kpv=0.05) is tested. Figs. 19 and 20 show the measured grid currents of inverters and bus voltages, respectively, where the stable operation of the power system is clearly observed. This matches well with the simulations results shown in Figs. 14

and 15 and further validates the impedance-based stability analysis in Fig. 11. Together with Figs. 17 and 18, the experimental tests points out that the interaction between the voltage control loop of the voltage-controlled inverter and the rest of network results in harmonic-frequency oscillations propagating into the power system.

VI. CONCLUSIONS

This paper has discussed a modeling and analysis procedure for the harmonic stability problem in AC power-electronics-based power systems. Two attractive stability analysis methods, i.e., the CCM and impedance-based approach have been briefly reviewed, and have found that the impedance-based approach provides a more computationally efficient and design-oriented analysis tool than the CCM. The impedance-based approach was expanded to a three-phase meshed and balanced network, where the harmonic instability resulted from the interactions of the inner control loops for the voltage- and current-controlled inverters was studied. A method for deriving impedance ratios was developed based on the system nodal admittance matrix. Time-domain simulations and experimental results have shown that the proposed approach could be a promising way to address the harmonic instability in AC power-electronics-based power systems.

REFERENCES

[1] F. Blaabjerg, Z. Chen, and S. B. Kjaer, "Power electronics as efficient interface in dispersed power generation systems," *IEEE Trans. Power Electron.*, vol. 19, no. 5, pp. 1184-1194, Sep. 2004.

[2] P. Brogan, "The stability of multiple, high power, active front end voltage sourced converters when connected to wind farm collector system," in *Proc. EPE* 2010, pp. 1-6.

[3] J. H. Enslin and P. J. Heskes, "Harmonic interaction between a large number of distributed power inverters and the distribution network," *IEEE Trans. Power Electron.*, vol. 19, no. 6, pp. 1586-1593, Nov. 2004.

[4] J. Rocabert, A. Luna, F. Blaabjerg, and P. Rodriguez, "Control of power converters in AC microgrids," *IEEE Trans. Power Electron.*, vol. 27, no. 11, pp. 4734-4749, Nov. 2012.

[5] E. Mollerstedt and B. Bernhardsson, "Out of control because of harmonics–An analysis of the harmonic response of an inverter locomotive," *IEEE Control Syst. Mag.,* vol. 20, no. 4, pp. 70-81, Aug. 2000.

[6] Z. Shuai, D. Liu, J. Shen, C. Tu, Y. Cheng, and A. Luo, "Series and parallel resonance problem of wideband frequency harmonic and its elimination strategy," *IEEE Trans. Power Electron.*, vol. 29, no. 4, pp. 1941-1952, Apr. 2014.

[7] N. Bottrell, M. Prodanovic, and T. C. Green, "Dynamic stability of a microgrid with an active load," *IEEE Trans. Power Electron.*, vol. 28, no. 11, pp. 5107-5119, Nov. 2013.

[8] N. Jelani, M. Molinas, and S. Bologani, "Reactive power ancillary service by constant power loads in distributed AC systems," *IEEE Trans. Power Del.*, vol. 28, no. 2, pp. 920-927, Apr. 2013.

[9] B. Wen, D. Boroyevich, P. Mattavelli, Z. Shen, and R. Burgos, "Experimental verification of the generalized Nyquist stability criterion for balanced three-phase AC systems in the presence of constant power loads," in *Proc. IEEE ECCE* 2012, pp. 3926-3933.

[10] T. Messo, J. Jokipii, J. Puukko, and T. Suntio, "Determining the value of DC-link capacitance to ensure stable operation of a three-phase photovoltaic inverter," *IEEE Trans. Power Electron.*, vol. 29, no. 2, pp. 665-673, Feb. 2014.

[11] J. M. Espi and J. Castello, "Wind turbine generation system with optimized dc-link design and control," *IEEE Trans. Ind. Electron.*, vol. 60, no. 3, pp. 919-929, Mar. 2013.

[12] L. Harnefors, M. Bongiorno, and S. Lundberg, "Input-admittance calculation and shaping for controlled voltage-source converters," *IEEE Trans. Ind. Electron.*, vol. 54, no. 6, pp. 3323-3334, Dec. 2007.

[13] B. Wen, D. Boroyevich, P. Mattavelli, Z. Shen, and R. Burgos, "Influence of phase-locked loop on input admittance of three-phase voltage-source converters," in *Proc. IEEE APEC* 2013, pp. 897-904.

[14] T. Messo, J. Jokipii, A. Makinen, T. Suntio, "Modeling the grid synchronization induced negative-resistor-like behavior in the output impedance of a three-phase photovoltaic inverter," in *Proc. IEEE PEDG* 2013, pp.1-8.

[15] E. A. Coelho, P. Cortizo, and P. F. Gracia, "Small signal stability for parallel-connected inverters in stand-alone ac supply systems," *IEEE Trans. Ind. Appl.*, vol. 38, no. 2, pp. 533-542, Mar./Apr. 2002.

[16] M. Marwali, J. W. Jung, and A. Keyhani, "Stability analysis of load sharing control for distributed generation systems," *IEEE Trans. Energ. Convers.*, vol. 22, no. 3, pp. 737-745, Sept. 2007.

[17] E. Barklund, N. Pogaku, M. Prodanvoic, C. H. Aramburo, and T. C. Green, "Energy management in autonomous microgrid using stability-constrained droop control of inverters," *IEEE Trans. Power Electron.*, vol. 23, no. 5, pp. 2346-2352, Sept. 2008.

[18] J. D. Ainsworth, "Harmonic instability between controlled static converters and a.c. networks," *Proc. Inst. Elect. Eng.*, vol. 114, pp.949-957, Jul. 1967.

[19] F. Wang, J. Duarte, M. Hendrix, and P. Ribeiro, "Modelling and analysis of grid harmonic distortion impact of aggregated DG inverters," *IEEE Trans. Power Electron.*, vol. 26, no. 3, pp. 786-797, Mar. 2011.

[20] R. Turner, S. Walton, and R. Duke, "Stability and bandwidth implications of digitally controlled grid-connected parallel inverters," *IEEE Trans. Ind. Electron.*, vol. 57, no. 11, pp. 3685-3694, Nov. 2010.

[21] L. Harnefors, L. Zhang, and M. Bongiorno, "Frequency-domain passivity-based current controller design," *IET Power Electron.*, vol. 1, no. 4, pp. 455-465, Dec. 2008.

[22] X. Wang, F. Blaabjerg, M. Liserre, Z. Chen, J. He, and Y. Li, "An active damper for stabilizing power-electronics-based AC systems," *IEEE Trans. Power Electron.*, Early Access Article, 2013.

[23] X. Wang, F. Blaabjerg, Z. Chen, and W. Wu, "Resonance analysis in parallel voltage-controlled distributed generation inverters," in *Proc. IEEE APEC* 2013, pp. 2977-2983.

[24] X. Wang, F. Blaabjerg, and Z. Chen, "Autonomous control of inverter-interfaced distributed generation units for harmonic current filtering and resonance damping in an islanded microgrid," *IEEE Trans. Ind. Appl.*, Early Access Article, 2013.

[25] M. Corradini, P. Mattavelli, M. Corradin, and F. Polo, "Analysis of parallel operation of uninterruptible power supplies loaded through long wiring cables," *IEEE Trans. Power Electron.*, vol. 25, no. 4, pp. 1046-1054, Apr. 2010.

[26] S. Zhang, S. Jiang, X. Lu, B. Ge, and F. Z. Peng, "Resonance issues and damping techniques for grid-connected inverters with long transmission cable," *IEEE Trans. Power Electron.*, vol. 29, no. 1, pp. 110-120, Jan. 2014.

[27] J. Agorreta, M. Borrega, J. Lopez, and L. Marroyo, "Modeling and control of *N*-paralleled grid-connected inverters with *LCL* filter coupled due to grid impedance in PV plants," *IEEE Trans. Power Electron.*, vol. 26, no. 3, pp. 770-785, Mar. 2011.

[28] L. H. Kocewiak, J. Hjerrild, C. L. Bak, "Wind turbine converter control interaction with complex wind farm systems," *IET Renew. Power. Gen.*, vol. 7, no. 4, pp. 380-389, Jul. 2013.

[29] Z. He, H. Hu, Y. Zhang, and S. Gao, "Harmonic resonance assessment to traction power-supply system considering train model in China high-speed railway," *IEEE Trans. Power Del.*, vol. PP, no. 99, pp. 1-9, Early Access Article, 2013.

[30] H. Lee, C. Lee, and G. Jang, "Harmonic analysis of the Korean high-speed railway using the eight-port representation model," *IEEE Trans. Power Del.*, vol. 26, no. 2, pp. 979-986, Apr. 2006.

[31] P. Kundur, *Power System Stability and Control*, McGraw-Hill Professional, 1994.

[32] N. Pogaku, M. Prodanovic, and T. C. Green, "Modeling, analysis and testing of an inverter-based microgrid," *IEEE Trans. Power Electron.*, vol. 22, no. 2, pp. 613-625, Mar. 2007.

[33] G. Gaba, S. Lefebver, and D. Mukhedkar, "Comparative analysis and study of the dynamic stability of AC/DC systems," *IEEE Trans. Power Syst.*, vol. 3, no. 3, pp. 978-985, Aug. 1988.

[34] S. Lefebver and R. Dube, "Control system analysis and design for an aerogenerator with eigenvalue methods," *IEEE Trans. Power Syst.*, vol. 3, no. 4, pp. 1600-1608, Nov. 1988.

[35] S. Lefebver, "Tuning of stabilizers in multi-machine power systems," *IEEE Trans. Power Appar. Syst.*, vol. PAS-102, no. 2, pp. 290-299, Feb. 1983.

[36] R. Middlebrook, "Input filter considerations in design and application of switching regulators," in *Proc. IEEE IAS'76*, pp. 366-382, 1976.

[37] M. Belkhayat. *Stability Criteria for AC Power Systems with Regulated Loads.* Ph.D. thesis, Purdue University, Dec. 1997.

[38] J. Sun, "Small-signal methods for AC distributed power systems–a review," *IEEE Trans. Power Electron.*, vol. 24, no. 11, pp. 2545-2554, Nov., 2009.

[39] R. Turner, S. Walton, and R. Duke, "A case study on the application of the Nyquist stability criterion as applied to interconnected loads and sources on grids," *IEEE Trans. Ind. Electron.*, vol. 60, no. 7, pp. 2740-2749, Jul. 2013.

[40] J. Sun, "Impedance-based stability criterion for grid-connected inverters," *IEEE Trans. Power Electron.*, vol. 26, no. 11, pp. 3075-3078, Nov., 2011.

[41] L. Harnefors, "Modeling of three-phase dynamic systems using complex transfer functions and transfer matrices," *IEEE Trans. Ind. Electron.*, vol. 54, no. 4, pp. 2239-2248, Aug. 2007.

[42] S. Buso and P. Mattavelli, *Digital Control in Power Electronics*, Morgen & Claypool Publishers, 2006.

[43] S. Hiti, D. Boroyevich, and C. Cuadros, "Small-signal modeling and control of three-phase PWM converters," in *Proc. IEEE IAS 1994*, pp. 1143-1150.

[44] Z. Yao, P. G. Therond, and B. Davat, "Stability analysis of power systems by the generalized Nyquist criterion," in *Proc. Int. Conf. CONTROL'94*, vol.1, pp. 739-744, Mar. 1994.

[45] A. MacFarlane and I. Postlethwaite, "The generalized Nyquist stability criterion and multivariable root loci," in *Int. Jour. of Control*, vol. 25, pp. 81-127, Jan. 1977.

[46] S. Lefebvre, D. P. Carroll, and R. A. DeCarlo, "Decentralized power modulation of multiterminal HVDC systems," *IEEE Trans. Power Appr. Syst.*, vol. PAS-100, no. 7, pp. 3331-3339, Jul. 1981.

[47] J. Yin, S. Duan, and B. Liu, "Stability analysis of grid-connected inverter with LCL filter adopting a digital single-loop controller with inherent damping characteristic" *IEEE Trans. Ind. Inform.*, vol. 9, no. 2, pp. 1104-1112, May 2013.

[48] S. K. Chung, "A phase tracking system for three phase utility interface inverters," *IEEE Trans. Power Electron.*, vol. 15, no. 3, pp. 431-438, May 2000.